The origin of nanoscale variations in photoresponse of an organic solar cell

Behrang H. Hamadani[*,1], Suyong Jung[1,2], Paul M. Haney[1], Lee J. Richter[3] and Nikolai B. Zhitenev[1]

[1]*Center for Nanoscale Science and Technology, National Institute of Standards and Technology, Gaithersburg, MD 20899*

[2]*Maryland NanoCenter, University of Maryland, College Park, MD 20742*

[3]*Chemical Science and Technology Laboratory, National Institute of Standards and Technology, Gaithersburg, MD 20899*

*behrang.hamadani@nist.gov

Received Date (will be automatically inserted after manuscript is accepted)

ABSTRACT

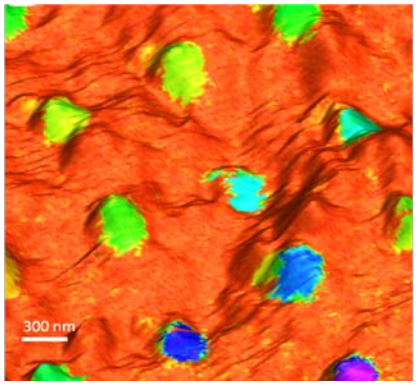

Abstract Photo generated charge transport in bulk heterojunction (BHJ) solar cells is strongly dependent on the active layer nanomorphology resulting from phase segregation. Here, we systematically study the nanoscale photocurrent response from BHJs based on poly(3-hexylthiophene) and phenyl-C61-butyric acid methyl ester (P3HT:PCBM) with a photoconductive atomic force microscope (PCAFM). The photocurrent is either collected directly by the tip or through nanopatterned metal contacts. The photoresponse measured at the top surface shows significant inhomogeneity on the length scale of 100 nm to 500 nm with large low-efficiency regions, consistent with existence of a P3HT-rich skin layer of ≈ 10 nm thick. The measurements with the nanocontacts validate the PCAFM results and demonstrate that the inhomogeneity averages to the conventional device result. Additionally, we use a ultra low angle microtomy (ULAM) technique to slice the active layer and create wedges along these cuts for probing of nanomorphology in the bulk. AFM images show a striking contrast between the top surface and the ULAM exposed material, revealing much finer features related to phase segregation below the skin layer and sub-100 nm length scales for charge transport.

Bulk heterojunction (BHJ) organic solar cells have shown significant improvement in performance over the last few years[1,2] and much effort is under way to further elucidate the photophysical phenomena and the mechanisms responsible for charge generation and transport in these systems.[3,4] Of particular interest is the role of the nanomorphology of the active layer on exciton dissociation and transport of free charge carriers to the collecting contacts. BHJs based on blends of P3HT and PCBM have attracted much attention since optimization of the solution deposition process[5] or annealing temperature[6] produce highly efficient devices. Improvements have often been associated with better active layer ordering in both the polymer and the fullerene regions, resulting in enhanced optical absorption and improved hole mobility.[1,7-9] Additionally, it was recently demonstrated that vertical phase segregation driven by minimization of the interface free energy in the P3HT:PCBM films can impact devices by accumulation of unfavorable regions at both the air or the buried interfaces.[10,11]

A variety of scanning probe techniques and microcopies have been employed to investigate the role of nanomorphology on charge transport in the organic photovoltaic (OPV) film. More insight is frequently obtained when structural characterizations are combined with optical or electrical measurements at the nanoscale. Conductive-tip AFM has been performed to investigate dark conductivities and local current-voltage variations in blended PV films.[12-14] Other scanning probe techniques employed to date include photoconductive AFM to study photocurrent variations due to film nanomorphology,[15,16] scanning Kelvin probe microscopy (SKPM) for studying the surface potential,[17-19] near-field scanning optical microscopy (NSOM) to investigate local photoluminescence or photocurrent,[20,21] and scanning transmission x-ray microscopy for studying of nanoscale chemical composition in these films.[22] Conductive AFM measurements, although extremely useful, currently have limitations stemming from the complicated nature of tip-sample contact. The typical, air-stable, metal-coated tips (Au or Pt) are not usually suitable to probe electron injection or collection from the electron conducting materials such as PCBM due to the large energetic mismatch between the metal Fermi level and the lowest unoccupied molecular orbital (LUMO).[23]

In this work, we utilize arrays of nanoscale silver (Ag) electrodes fabricated directly on top of the active layer without lithographic patterning on the sensitive organic film to probe the local photoresponse. Next, we compare photoconductive AFM (PCAFM) with the nanodevice measurements. Although the microscopic nature of the contact interface cannot be the same, we find that PCAFM data obtained with a conductive diamond tip, with work function similar to that of Ag, closely resemble the characteristics of the nanodevices. The nanocontact data and photoconductive AFM maps both consistently reveal that high efficiency electron collection is limited to sparse hot spots. The film bulk exposed by the ultra low angle microtome display much finer structures well below 100 nm and a more blended photocurrent data.

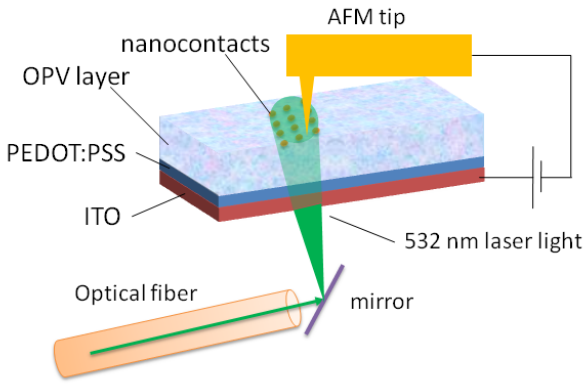

Figure 1. Schematics of the photoconductive AFM setup.

Blended P3HT:PCBM (1:1) films were prepared by spin-coating followed by solvent and heat annealing of the film on Poly(3,4-ethylenedioxythiophene) poly(styrenesulfonate) (PEDOT:PSS) coated indium tin oxide (ITO) electrodes. We employ a fabrication recipe known to produce highest efficiency devices (see supporting documents). The active layer film thickness was typically around 140 nm as verified by spectroscopic ellipsometry and profilometry. Devices with mm-sized top and bottom electrodes (top electrode: Ca/Ag (40/100 nm)) were fabricated and measured separately on similarly prepared films, showing excellent *I-V* characteristics (FF=60 %, J_{SC}=11 mA cm^{-2}, V_{OC}=0.6 V, where FF is the fill factor, J_{SC} is the short circuit current density and V_{OC} is the open circuit voltage) with power conversion efficiencies of ≈ 4 % under AM 1.5G illumination conditions as determined by a National Renewable Energy lab (NREL) traceable silicon reference solar cell without correction for the calibration mismatch factor.[24]

The nanoscale contacts were deposited by metal evaporation through silicon nitride stencil masks with arrays of small openings in the shape of dots as defined by e-beam lithography and an etch process.[25]. The completed stencil mask can be used for several metal evaporations until significant clogging of the holes occurs. The nanodot arrays were designed with different diameters with the smallest nanodots on the OPV film formed with 300 nm diameter openings. We note that the nucleation and growth of metals on organic films are generally dependent on a variety of factors[26] such as the sticking coefficient and the evaporation rate and this may be further complicated by the constricted geometry of the masks. The yield of successful Ag nanodot formation was about 30 %. We avoided using Au, Pt or other high work function materials because their use as cathode electrodes in devices results in poor open circuit voltage and low photogenerated current. We chose Ag over other lower work function metals such Al or Ca because it oxidizes at a much slower pace and the reproducibility of the nanodevices was better. The AFM tip used for probing of

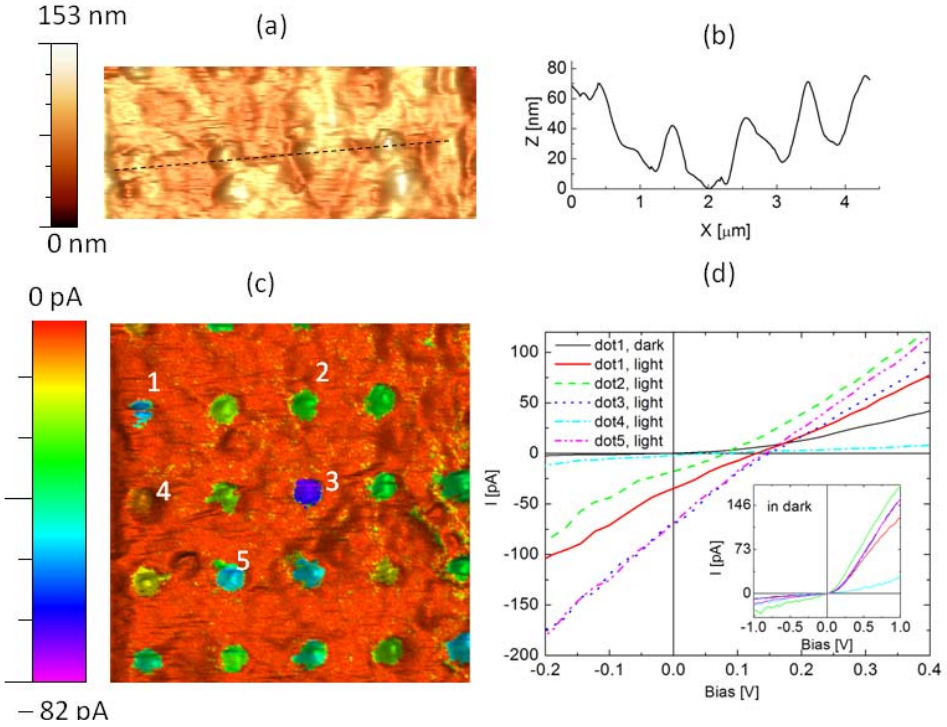

Figure 2. (a) A section of an AFM scan of the OPV films with a thermally evaporated silver nanodot array with an average dot diameter of ≈ 300 nm. (b) A line scan corresponding to the dashed line in (a) over a segment of the nanodot array (c) Photo response of the 300 nm nanodot array under the short circuit illumination conditions with the photocurrent color-coded map superimposed directly on top of the 3-D topography data. The scan size is 4.5 μm × 4.5 μm. (d) (Inset) Dark I-V characteristics of five random nanodots as marked on the graph. (Main) I-V characteristics of the same devices under illumination.

the nanodots is a boron-doped conductive diamond-coated tip. In addition to its excellent wear properties, we find that it exhibits a work function similar to that of Ag, based on similar V_{OC}.

The schematic of the photoconductive AFM measurement is shown in Fig. 1 and discussed in more detail in the supporting document. All measurements were performed in a dry, N_2 environment. Estimated laser power levels at the sample were ~ 2W cm^{-2}. Figure 2a shows a section of an AFM scan of the surface of the OPV film prepared as described above and with the deposition of a silver nanodot array through the shadow mask (with a line scan in Fig. 2b) with an average dot diameter of ≈ 300 nm and height of 40 nm. The image is a 3-D graphical rendering of the surface with tilt and rotation set to zero. The surface topography by itself is very rough with peak to valley variations of up to 40 % of the total film thickness. This roughness is the result of the low spin rate from a hot solvent and the slow drying of the film under the solvent anneal process.[1] In Fig. 2c, we show the photocurrent response of the nanodots under the short circuit conditions with the photocurrent color-coded map superimposed directly on top of the 3-D topography data. Among different dots, a significant variation (up to a factor of 10) in photocurrent response is observed. We do not find any consistent correlation between the topography and the photocurrent data suggesting that the variations in the material organization that gives rise to the topographical features have only minor effects on device performance. The variations in the nanodot photoresponse is not related to the tip/nanodot contact quality as repeated scans over the same area and other arrays of nanodots produce identical results. Current-voltage characteristics from several of these dots in the dark are shown in the inset of Fig. 2d. Most show relatively well-behaved diode-like response with low reverse saturation currents and high forward bias currents (substrate bias with respect to the tip). The main panel of Fig. 2d shows the *I-V* characteristics under illumination. With the bias voltage applied to the ITO film and the polarity of the V_{OC} as obtained (positive V_{OC} and photocurrent crossing from negative to positive), the electrons are collected from the top while holes reach the ITO, similar in behavior to large-scale devices. Since electrons are accepted and transported via PCBM networks, the data suggest that the nanodots with the greatest response are in intimate contact with PCBM regions near the surface.

The nanodots exhibit a nearly linear photoresponse in reverse bias (FF of ≈ 25 %). While this has been associated with recombination losses due to low dissociation efficiency of bound electron-hole pairs in other OPV systems,[27,28] we attribute it to the high illumination intensities necessary to observe robust (pA) currents on the nanoscale and the role of the ever-present finite series resistance. In order to perform a careful study

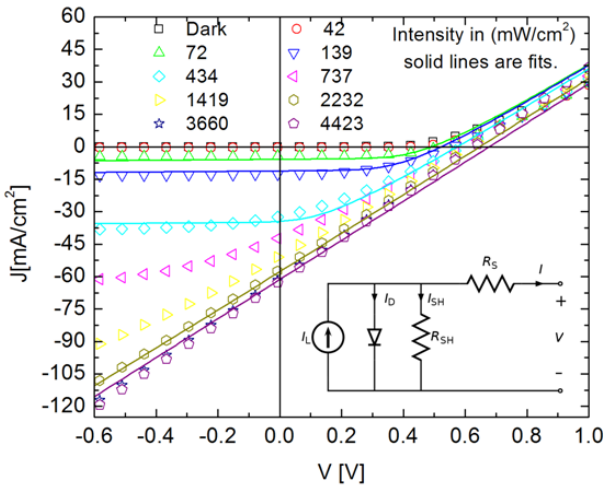

Figure 3. Current density vs. voltage for a mm-sized device (2 mm × 2 mm area) at several illumination intensities. At extremely high intensities, the I-V characteristics show linear behavior. Solid lines are fits to data using the equivalent circuit model shown. Fitting parameters: $J_0(I_0/A) = 8.27\times10^{-4}$ A m^{-2}, $R_s.A = 0.00109$ Ω m^2, $R_{sh}.A = 0.0924$ Ω m^2, n =1.77, and J_L = 0.8125/ Intensity (A/m^2)/(mW/cm^2).

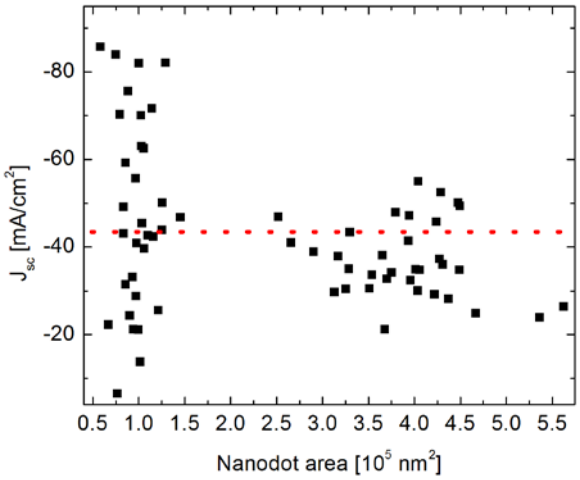

Figure 4. Short circuit current density (J_{SC}) as a function of the nanodot area for a variety of nanocontacts, showing large fluctuations for smaller dots.

of this phenomenon, we independently measured the *I-V* characteristics of a mm-sized device with a Ca/Ag cathode as a function of light intensity (with a solar simulator), and the data are shown in Fig. 3. As the light intensity increases, the FF is reduced and the reverse bias dependence of the current becomes more significant. At intensities of about 1 W cm^{-2} (10 suns) and higher, the *I-V* curves look approximately linear with FF reduced to 25 % (from 70 % at low intensities), all very consistent with the nanodot *I-V* characteristics at the laser illumination intensities of the experiment (≈ 2 W cm^{-2} (20 suns)). Additionally, the limiting magnitude of the J_{SC} (=I_{SC}/A, where A is the area) of 60 mA cm^{-2} is within the range of the average nanodot current density as described below. This transition from light-shifted diode-like behavior to linear behavior is captured with an equivalent circuit (EC) model drawn in the inset of Fig. 3. In its simplest form, this model consists of a diode (with reverse saturation current, I_0, and ideality factor n) in parallel with a current source generating current I_L and representing the active solar cell. This "diode solar cell" is in parallel with a shunt resistance R_{sh}, capturing shorting of the circuit, and in series with a series resistance R_s. The current voltage relation is given by[29]

$$I(V) = -I_L + I_0\left(\exp\left(\frac{q(V-IR_s)}{nkT}\right)-1\right)+\frac{V-IR_s}{R_{sh}} \quad (1).$$

We assume that the current I_L is proportional to the illumination intensity and extract the constant of proportionality from the low intensity data. With this relation, the other parameters of the model are obtained using a non-linear least-square fit to all of the data of Fig. 3. We find good agreement over all illumination intensities with the parameters of the fit given in the caption of Fig. 3.

A detailed analysis of nanodot photoresponse vs. size shows that as the nanodots size increases, the fluctuations in the short circuit current density among different dots are reduced. This can be seen clearly in Fig. 4, where the J_{SC} from several scans over variety of arrays is plotted as a function of the nanodot area. For small size nanodot arrays, the fluctuations can be as large as a factor of 10, while fluctuations are reduced as the dot sizes grow, indicating an averaging that takes place over areas of high and low current. We find an average current density of −43 mA cm^{-2} under our illumination conditions (≈ 2 W cm^{-2} or 20 suns) for all types of dot arrays (300 nm, 500 nm, 600 nm). These numbers are consistent with large contact device parameters at high intensity.[30]

We attribute the origin of the fluctuations in the nanodot response to the nanomorphology of the film *surface*. In order to exclude the possibility that the variation arises from degradation of the Ag nanodots (in Ag devices, V_{OC} as low as observed here has been attributed to oxidation of the cathode[23]) we have performed direct photocurrent measurements with the AFM tip. The diamond-coated tips used for transport measurements from the nanodots work very well for direct contact and photocurrent measurements from the bare OPV film. We also experimented with Pt coated tips but were not able to collect good images under short circuit conditions, although the photocurrent images improve under large reverse bias. We attribute the good PCAFM images to the relatively low work function (4.1±0.5 eV grown on (111)-oriented substrates)[31] of the boron-doped diamond tips resulting in better band alignment for electron photocurrent collection from the PCBM regions (with LUMO position estimated at ≈ 4.0 eV)[23]. Figure 5a shows a 3-D plot of the film topography overlaid with the photocurrent map collected simultaneously with a conductive diamond-coated AFM tip under illumination at short circuit conditions. Consistent with the previous observations on the nanodots, we do not observe any

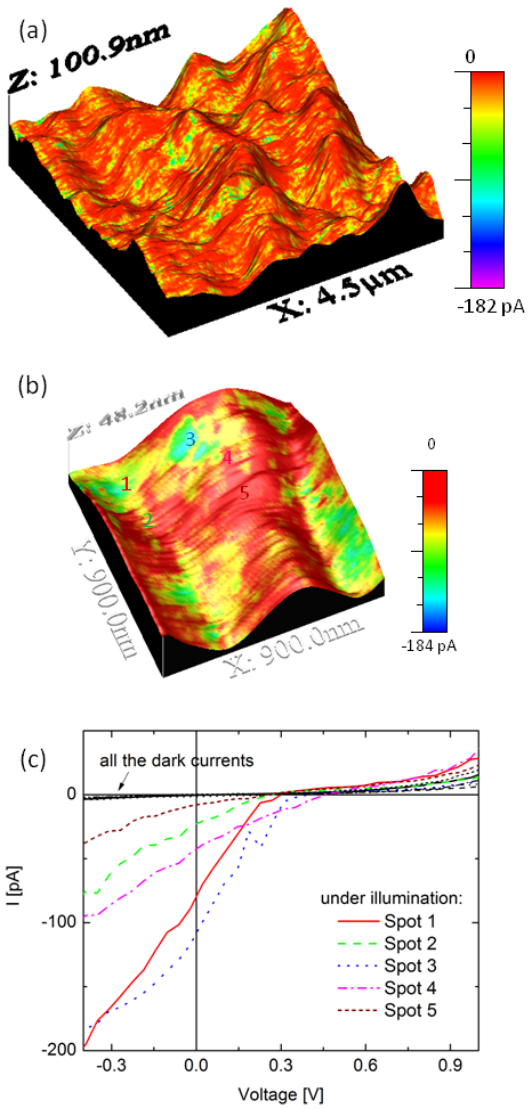

Figure 5. (a) 3-D plot of the film topography overlaid with the photocurrent map collected simultaneously with a conductive diamond-coated AFM tip under short circuit conditions. (b) a smaller scanned area with locations of local I-V measurements in (c)

specific correlation between topography and photoconductive response, i.e., areas of low or high current are observed throughout the film without a clear topographical correlation. Similar lack of topographic correlation has been observed in earlier PC-AFM studies.[16] It is noted however that since the tip radius of curvature is very large (≈ 100 nm), topographical features appear smooth in the scans, but photocurrent features as small as 50 nm can be detected. The variations in photocurrent are large and can be as high as an order of magnitude of change over lateral dimensions as small of as 100 nm. In this regard, largest photocurrent is observed in small regions which we refer to as "hot spots" of current on the order of tens of nm, occasionally growing in size up to 200 nm. In between the hot-spot regions (green and blue) there are regions of intermediate conductance (yellow color) that can extend larger in size, but the majority of film surface is relatively non-photoconductive (red). A flooding analysis of this image

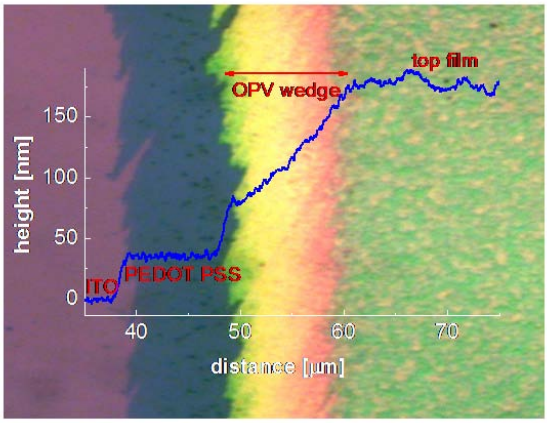

Figure 6. An optical micrograph of the OPV wedge region and a line scan data obtained by a profilometer. The purple region is the exposed ITO surface where the film is completely removed. Farther to the right is a dark green region corresponding to the PEDOT PSS layer, followed by the color-shifted OPV region on top of the PEDOT layer. The rough region on the far right is the top of the OPV film.

reveals that the total area of the photocurrent response above the floor noise (yellow through violet) only constitutes (20 to 30) % of the total area of the film. As with the nanodots, from the polarity of V_{OC} and the sign of I, we observe that the photogenerated holes are collected from the ITO contact and electrons, transported via the PCBM networks, are collected at the top surface with the AFM tip; therefore, the hot spots are expected to originate from transport of electrons by PCBM regions to the tip. Our results suggest that only about 25 % of the free (air) surface of the OPV film is enriched with PCBM. This is quantitatively consistent with near-edge x-ray absorption fine structure (NEXAFS) spectra of the free surface of identically processed films.[11] Statistical analysis of the data of Fig. 5a by construction of an "imaginary" nanodot array on that surface based on integrating the local photocurrent response over regions of fixed area leads to photoresponse variations very similar to those shown in Fig. 2c with "real" contacts (see supporting documents for an example).

Figure 5b shows a smaller scanned area of another film with similar characteristics as described above. We have performed local *I-V* measurements of different colored-regions and the results are plotted in Fig. 5c. The reverse-bias dependence of the current and the low FFs are similar to nanodot data and are attributed to the large illumination intensities coupled with the series resistance. Open circuit voltages in the range of 0.3 V to 0.45 V are very similar to those observed in macroscopic devices fabricated with Al top contacts[23], further validating that the diamond tip work function is similar to Al. Some low-conductance regions of the film show a superlinear increase of negative current with reverse bias which has been reported in blends of devices with low-acceptor loading.[32] The *I-V* data also reveal very high series resistances (R_S) in the forward bias as evident from the very slow increase of current with voltage beyond the V_{OC}. In general, the lower photocurrent regions show more nonideal *I-V* characteristics. The dark currents for all the spots are also

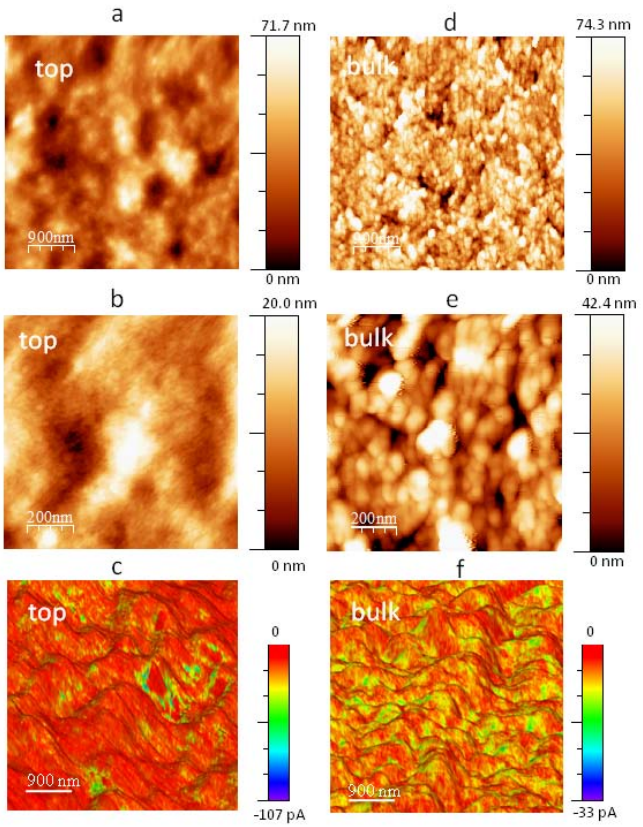

Figure 7. High-resolution intermittant-contact AFM images of the top OPV film (a and b), and the bulk of the film from the wedge region (d and e). (c and f) Color-coded photocurrent data superimposed on 3D-rendering of topography scans for the top film (c) and bulk (f) as imaged by the diamond tip. Bulk photoresponce is measured under a small substrate bias of –0.3 V for improved signal to noise.

shown in the plot and demonstrate better diode-like characteristics, i.e., higher shunt resistance but the series resistance remains comparable to the *I-V* under light. We believe that the high series resistance (lack of strong turn-on beyond the V_{OC}) is due to the large contact resistances between the tip and the sample. In this regard, we see that R_S for PCAFM is significantly higher than that measured from the nanodots. For example, for dot #5 in Fig 2c, we obtain an R_S of 2 Ω cm^2 which is roughly a factor of 10 lower than the best *I-V* results taken directly with the diamond-coated tip (19 Ω cm^2 assuming a tip radius of curvature of 150 nm as noted in the manufacturer's datasheet).

The PCAFM results from the top surface are consistent with an electron blocking skin (P3HT) with lateral scale of hundreds of nm and dilute hot spots corresponding to PCBM nanocrystals on or near the top surface. The current does not appear to directly reflect the bulk morphology, which recent TEM tomography studies have revealed to exhibit much finer structures and a more uniform blending.[8,9] In an attempt to access the bulk nanomorphology, we have used ULAM to make cuts in the OPV film, removing the surface layer and creating exposed wedges along the cut directions (more details in the supplemental data). Figure 6 shows an optical micrograph of one such cut and a profilometer line scan data along the cut. The nature of each exposed layer has

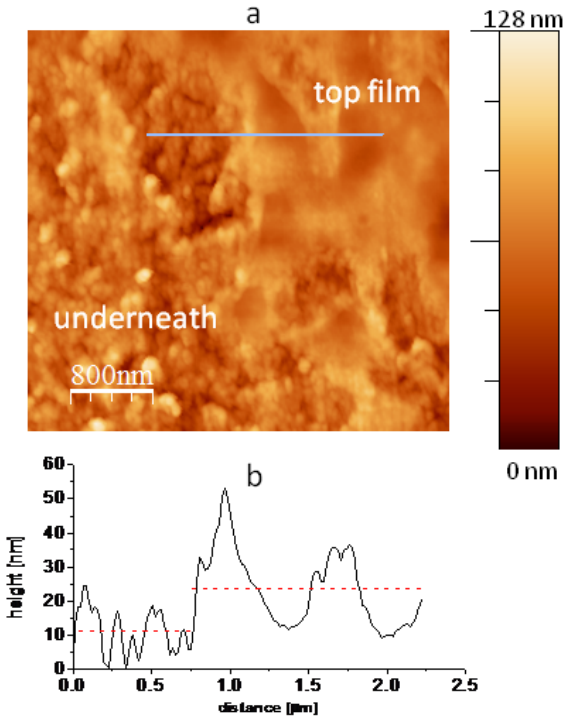

Figure 8. a) A high-resolution AFM scan near the top of the wedge showing the sharp transition from the bulk morphology to the top skin layer of the film. b) a line scan across the two regions showing an average step of ≈ 10 nm corresponding to the removed skin layer.

been verified by careful high-resolution AFM imaging along the slice. The profile indicates regions of uniform adhesive failure at the ITO/PEDOT:PSS interface (purple) and, failure near the PEDOT:PSS/BHJ interface (blue). There is a region (yellow) of almost 80 nm in height over a distance of (10 to 12) μm that produces a monotonic wedge indicative of uniform cohesive failure in the BHJ layer, allowing us to image the bulk structure below the surface.

In Figures 7a and 7b, high-resolution intermittent contact AFM images of the top of the film with a Si_3N_4 tip with 10 nm radius of curvature are shown consistent with AFM scans of similarly prepared films in the literature. Figures 7d and 7e show scans from the wedge region with much finer morphology. These images clearly show that the top morphology that is enriched with a P3HT skin layer as evident from our PCAFM data and independently demonstrated by XPS and NEXAFS measurements, does not represent the material blending in the bulk. A clear transition from the bulk to the top layer morphology can be observed in the high-resolution AFM image of Fig. 8a, where an area near the top of the wedge is scanned. The bulk morphology transitions rather abruptly into the top film morphology, suggesting that the skin layer is very thin. From several line scans (Fig. 8b) along this transition region, we estimate that the top layer thickness is ≈ 10 nm or less.

The topology of the exposed wedges is suggestive of cohesive fracture of the film. The relationship between this surface and the initial bulk morphology is complex

and clearly requires future investigation. We have explored the exposed topology as a function of ULAM conditions (room temperature and cryogenic) for both the films presented here and films prepared with an alternative recipe that produces a more disordered morphology leading to lower device performance. The high-resolution AFM images from these experiments, which are described in more detail in the supplementary section, revealed that the ULAM is robust with conditions and clearly reflects differences in the bulk nanomorphology between the two films.

Figures 7c and 7f show PCAFM data from the top and the bulk region, respectively and show that without the top skin layer, the bulk photoresponse is much more uniform across the film, although the low resolution of the diamond tip (100 nm radius of curvature) does not allow us to assign one material phase or another to topographically fine features observed in Fig. 7d. This confirms that the skin layer is directly responsible for low photocurrent yield from large areas of the top surface. The high external quantum efficiency (peaking around 60 %) and conversion efficiency of these cells suggest that the hot spots in the surface are adequate to harvest the majority of the bulk carriers, i.e. the length scales of the surface contacts do not represent that of lateral bulk transport.

In conclusion, we have combined the fabrication of nanoscale contacts with a photoconductive scanning probe microscope to understand the role of morphology on photocurrent transport in high-performance blended P3HT: PCBM films. Both nanoscale contacts and the probing tip measurements demonstrate a very inhomogeneous response with a low density of high-efficient hot spots emanating from an enrichment of the top surface with P3HT. Removal of the top layer by ULAM and probing of the bulk morphology with high-resolution microscopy confirm that the gross inhomogeneities are due to the surface and do not reflect the bulk organization. Our results are consistent with published spectroscopic data revealing an abundance of polymer species at the air/OPV interface, and tomography data showing fine blending within the bulk.

Acknowledgment The authors would like to thank Amit Agrawal, Henry Lezec, J. Alexander Liddle, and David Gundlach for useful discussions, and Dean DeLongchamp for use of film preparation equipment. This work has been made possible with the tools and staff support of the nanofabrication research facility at the Center for Nanoscale Science and Technology.

Supporting Information Available Fabrication details and film and device preparation, including schematics and an image of SiN membrane mask. Some statistical analysis data and additional ULAM images.

References

(1) Li, G.; Shrotriya, V.; Huang, J.; Yao Y.; Moriarty, T.; Emery, K.; Yang, Y. High-efficiency solution processable polymer photovoltaic cells by self-organization of polymer blends. *Nat. Mater.* **2005**, *4*, 864-868.

(2) Peet, J.; Kim, J. Y.; Coates, N. E.; Ma, W. L.; Moses, D.; Heeger, A. J.; Bazan, G. C.. Efficiency enhancement in low-bandgap polymer solar cells by processing with alkane dithiols. *Nat. Mater.* **2007**, *6*, 497.

(3) Ohkita, H.; Cook, S.; Astuti, Y.; Duffy, W.; Tierney, S.; Zhang, W.; Heeney, M.; McCulloch, I.; Nelson, J.; Bradley, D. D. C.; Durrant, J. R. Charge carrier formation in polythiophene/fullerene blend films studied by transient absorption spectroscopy. *J. Am. Chem. Soc.* **2008**, *130*, 3030.

(4) Uhrich, C.; Wynands, D.; Olthof, S.; Riede, M. K.; Leo, K.; Sonntag, S.; Maennig, B.; Pfeiffer, M. Origin of open circuit voltage in planar and bulk heterojunction organic thin-film photovoltaics depending on doped transport layers. *J. Appl. Phys.* **2008**, *104*, 043107.

(5) Li, G.; Yao, Y.; Yang, H.; Shrotriya, V.; Yang, G.; Yang, Y. "Solvent annealing" effect in polymer solar cells based on poly(3-hexylthiophene) and methanofullerenes. *Adv. Funct. Mater.* **2007**, *17*, 1636.

(6) Ma, W.; Yang, C.; Gong, X.; Lee, K.; Heeger, A. J. Thermally stable, efficient polymer solar cells with nanoscale control of the interpenetrating network morphology. *Adv. Funct. Mater.* **2005**, *15*, 1617.

(7) Yang, X.; Loos, J.; Veenstra, S. C.; Verhees, W. J. H.; Wienk, M. M.; Kroon, J. M.; Michels, M. A. J.; Janssen, R. A. J. Nanoscale morphology of high-performance polymer solar cells. *Nano. Lett.* **2005**, *5*, 579.

(8) van Bavel, S. S.; Sourty, E.; de With, G.; Loos, J. Three-dimensional nanoscale organization of bulk heterojunction polymer solar cells. *Nano. Lett.* **2009**, 9, 507.

(9) van Bavel, S. S.; Sourty, E.; de With, G.; Frolic, K.; Loos, J. Relation between photoactive layer thickness, 3D morphology, and device performance in P3HT/PCBM bulk-heterojunction solar cells. *Macromolecules.* **2009**, 42, 7396.

(10) Xu, Z.; Chen, L-M.; Yang, G.; Huang, C-H.; Hou, J.; Wu, Y.; Li, G.; Hsu, C-S.; Yang, Y. Vertical phase separation in poly(3-hexylthiophene): fullerene derivative blends and its advantage for inverted structure solar cells. *Adv. Funct. Mater.* **2009**, *19*, 1.

(11) Germack, D. S.; Chan, C. K.; Hamadani, B. H.; Richter, L. J.; Fischer, D. A.; Gundlach, D. J.; DeLongchamp, D. M. Substrate-dependent interface composition and charge transport in films for organic photovoltaics. *Appl. Phys. Lett.* **2009**, *94*, 233303.

(12) Douhéret, O.; Lutsen, L.; Swinnen, A.; Breselge, M.; Vandewal, K.; Goris, L.; Manca, J. Nanoscale electrical characterization of organic photovoltaic blends by conductive atomic force microscopy. *Appl. Phys. Lett.* **2006**, *89*, 032107.

(13) Alexeev, A.; Loos, J.; Koetse, M. M. Nanoscale electrical characterization of semiconducting polymer blends by conductive atomic force microscopy (C-AFM). *Ultramic.* **2006**, *106*, 191.

(14) Dante, M.; Peet, J.; Nguyen, T-Q. Nanoscale charge transport and internal structure of bulk heterojunction conjugated polymer/fullerene solar cells by scanning probe microscopy. *J. Phys. Chem. C.* **2008**, *112*, 7241.

(15) Coffey, D. C.; Reid, O. G.; Rodovsky, D. B.; Bartholomew, G. P.; Ginger, D. S. Mapping local photocurrents in polymer/fullerene solar cells with photoconductive atomic force microscopy. *Nano Lett.* **2007**, *7*, 738.

(16) Pingree, L. S. C.; Reid, O. G.; Ginger, D. S. Imaging the evolution of nanoscale photocurrent collection and transport networks during annealing of polythiophene/fullerene solar cells. *Nano Lett.* **2009** (in press).

(17) Chiesa, M.; Bürgi, L.; Kim, J-S.; Shikler, R.; Friend, R. H.; Sirringhaus, H. Correlation between surface photovoltage and blend morphology in polyfluorene-based photodiodes. *Nano. Lett.* **2005**, *5*, 559.

(18) Maturova, K.; Kemerink, M.; Wienk, M. M.; Charrier, D. S. H.; Janssen, R. A. J. Scanning kelvin probe microscopy on bulk heterojunction polymer blends. *Adv. Funct. Mater.* **2009**, *19*, 1379.

(19) Liscio, A.; De Luca, G.; Nolde, F.; Palermo, V.; Mullen, K.; Samori, P. Photovoltaic charge generation visualized at the nanoscale: A proof of principle. *J. Am. Chem. Soc.* **2008**, *130*, 780.

(20) Chappell, J.; Lidzey, D. G.; Jukes, P. C.; Higgins, A. M.; Thompson, R. L.; O'Connor, S.; Grizzi, I.; Fletcher, R.; O'Brien, J.; Geoghegan, M.; Jones, R. A. L. Correlating structure with fluorescence emission in phase-separated conjugated-emission in phase-separated conjugated-polymer. *Nat. Mater.* **2003**, *2*, 616.

(21) Riehn, R.; Stevenson, R.; Richards, D.; Kang, D-J.; Blamire, M.; Downes, A.; Cacialli, F. Local probing of photocurrent and photoluminescence in a phase-separated conjugated-polymer blend by means of near-field excitation. *Adv. Funct. Mater.* **2006**, *16*, 469.

(22) McNeill, C. R.; Watts, B.; Thomsen, L.; Belcher, W. J.; Greenham, N. C.; Dastoor, P. C. Nanoscale quantitative chemical mapping of conjugated polymer blends. *Nano Lett.* **2006**, *6*, 1202.

(23) Reese, M. O.; White, M. S.; Rumbles, G.; Ginley, D. S.; Shaheen, S. E. Optimal negative electrodes for poly(3-hexylthiophene): [6,6]-phenylC61-butyric acid methyl ester bulk heterojunction photovoltaic devices. *Appl. Phys. Lett.* **2008**, *92*, 053307.

(24) Kroon, J. M.; Wienk, M. M.; Verhees, W. J. H.; Hummelen, J. C. Accurate efficiency determination and stability studies of conjugated polymeryfullerene solar cells. *Thin Solid Films* , **2002**, *403-404*, 223.

(25) Deshmukh, M. M.; Ralph, D. C.; Thomas, M.; Silcox, J. Nanofabrication using a stencil mask. *Appl. Phys. Lett.* **1999**, *75*, 1631.

(26) Zaporojtchenko, V.; Strunskus, T.; Behnke, K.; Bechtolshim, C. V.; Thran, A.; Faupel, F. Formation of metal-polymer interfaces by metal evaporation: influence of deposition parameters and defects. *Microelec. Eng.* **2000**, *50*, 465.

(27) Mandoc, M. M.; Veurman, W.; Koster, L. J. A.; de Boer, B.; Blom, P. W. M. Origin of the reduced fill factor and photocurrent in MDMO-PPV:PCNEPV all-polymer solar cells. *Adv. Funct. Mater*. **2007**, 17, 2167.

(28) Moliton, A.; Nunzi, J-M. How to model the behaviour of organic photovoltaic cells. *Polym. Int.* **2006**, *55*, 583.

(29) Sze, S. M. Semiconductor Devices. *Wiley*, New York, **1985**.

(30) Leever, B. J.; Durstock, M. F.; Irwin, M. D.; Hains, A. W.; Marks, T. J.; Pingree, L. S. C.; Hersam, M. C. Spatially resolved photocurrent mapping of operating organic photovoltaic devices using atomic force photovoltaic microscopy. *Appl. Phys. Lett.* **2008**, *92*, 013302.

(31) Geis, M. W.; Gregory, J. A.; Pate, B. B. Capacitance-voltage measurements on metal-SiO_2-diamond structures fabricated with (100)- and (111)-oriented substrates. *IEEE. Trans. Electron Devices*, **1991**, 38, 619.

(32) Qiao, F.; Liu, A.; Zhou, Y.; Xiao, Y.; Yang, P. O. Bulk heterojunction organic solar cell based on a novel fluorescent fluorine-boron complex. J. Mater. Sci. **2009**, 44, 1283.